NASA-CR-200906

A COMPARISON OF COMPUTED AND EXPERIMENTAL FLOWFIELDS OF THE RAH-66 HELICOPTER

Final Report NCC2-5137

C.P. van Dam
A.M. Budge
Department of Mechanical & Aeronautical Engineering,
University of California-Davis, Davis,CA

E.P.N. Duque
US Army Aeroflightdynamics Directorate, ATCOM, AVRDEC, Moffett Field, CA

Abstract

This paper compares and evaluates numerical and experimental flowfields of the RAH-66 Comanche helicopter. The numerical predictions were obtained by solving the Thin-Layer Navier-Stokes equations. The computations use actuator disks to investigate the main and tail rotor effects upon the fuselage flowfield. The wind tunnel experiment was performed in the 14x22 foot facility located at NASA Langley. A suite of flow conditions, rotor thrusts and fuselage-rotor-tail configurations were tested. In addition, the tunnel model and the computational geometry were based upon the same CAD definition. Computations were performed for an isolated fuselage configuration and for a rotor on configuration. Comparisons between the measured and computed surface pressures show areas of correlation and some discrepancies. Local areas of poor computational grid-quality and local areas of geometry differences account for the differences. These calculations demonstrate the use of advanced Computational Fluid Dynamic methodologies towards a flight vehicle currently underdevelopment. It serves as an important verification for future computed results.

Introduction

The flowfield around helicopters are so complicated that few have attempted to perform Navier-Stokes flowfield simulations of these aircraft. In comparison, the fixed wing community has performed numerous full airframe configuration computations over the past few years. The helicopter's more complicated flowfield has limited the use of numerical simulations.

The flowfield around helicopter fuselages have been computed using methods of varying resolution, approximations and accuracy. Each methodology has an associated computational requirement and set-up cost/benefit. Generally speaking, as approximations to the actual flow field increases, the computation and set-up cost decreases. Therefore, relatively low cost methods such as linear panel methods have been used extensively in industry in comparison to Navier-Stokes methods.

The RAH-66 (Comanche) helicopter is an important vehicle to the U.S. Army. It has been in development for the past several years and will have its first flight some time this Fall. To support its development, the U.S. Army Aeroflightdynamics Directorate formed a collaborative Computational Fluid Dynamics (CFD) and wind tunnel test program. The CFD and wind-tunnel tests were designed to provide complementary flowfield data. Both methods use geometry based on the same CAD database. Tunnel test conditions, pressure tap locations and laser velocimeter data were all designed to facilitate CFD verification and to maximize the use of the two types of flow field information.

CFD results were obtained and reported in an earlier work by Duque and Dimanlig[1]. Their work showed the use of a Navier-Stokes method with overset grids to compute the flowfield of an earlier Comanche fuselage design. Although they did not show comparison between computation and experiment, they did illustrate the capability to compute the flowfield of complicated helicopter fuselages.

The work presented in this paper will present the first comparison of CFD derived results of the RAH-66 (Comanche) helicopter to wind-tunnel data. The paper first gives a description of the experiment, the flow conditions and the two conditions for comparison. The computational method is then explained including the grid system used, the flow solver and some statistics on computational costs. The comparisons between the measured and computed are then presented. These preliminary comparisons show

some favorable comparisons and some local areas of discrepancies. The discrepancies between the computation and measured pressures can be explained by either poor grid quality or differences in geometry.

Experiment

The wind tunnel tests were performed at the 14x22 foot tunnel located at NASA Langley Research Center. The tunnel model, Figure 1, consists of a 15% scale model of the Comanche fuselage with a 4 bladed rotor and powered fan-tail. A suite of flow conditions, rotor thrusts and fuselage-rotor-tail configurations were tested. The model had approximately 200 surface pressure taps distributed along the fuselage. The taps were configured at station cuts on the fuselage, along the symmetry line on both the ventral (bottom) and dorsal (top) fuselage surfaces. Additional pressure taps were placed in the vicinity of the fan-tail. For the fan-tail, flowfield velocity measurements were taken along a grid on the inlet side using Laser Velocimetry (LV) and Doplar Global Velocimeter (DGV) techniques as shown in Figure 2. Force balance data was collected independently for the fuselage and the rotor system.

Two tunnel runs were chosen from the available data and summarized in the following table. The first case is an isolated fuselage with a corresponding freestream Mach number of 0.13, a Reynolds number of 989,000 based on overall fuselage length and at a fuselage angle-of-attack of 0.0 degrees. The fuselage angle-of-attack is based on the CAD geometry definition with 5 degrees of rotor shaft tilt. The second flow condition was a rotor on configuration. The freestream was set to an angle-of-attack of 0.737. The Mach number was 0.05 corresponding to a Reynolds number of 367,896 based on fuselage length. The rotor thrust coefficient (C_{TRotor}) was 0.00509. Both conditions had the fan-tail powered. Estimates of the fan-tail thrust were obtained from the fuselage force balance data and were approximately 18.35 pounds-force.

Table 1: Selected Tunnel Flow Conditions
Fan Thrust = 18.5 lbs_f

	Mach	Rey #	α (deg.)	C_{Trotor}
Case 1	0.13	989,000	0	n/a
Case 2 μ=0.076	0.05	389,000	-.737	0.00509

Computational Method

Grid System

The grid system is an overset grid system as discussed in the earlier work [1]. The body conforming grids were generated using the HYPGEN[4] code and the surface grids were generated using GRIDGEN2D[3], S3D[2], and ICEM/CFD. All grid connectivity information was obtained using the PEGASUS[5] code.

The current surface geometry is an accurate representation of the Comanche fuselage's CAD definition and matches the lines of the wind tunnel 15% scale model. Grid modifications required a complete re-griding of the previous CFD model. Figure 3 illustrates the modified surface geometry showing an overall representation of the surface and field grids and detailed figures of the EOSS and the Fan-Tail assembly. The grid system totaled 30 grids with the rotor actuator disk and approximately 3 million points. Figure 3a shows some overall grid features.

The grid around the nose of the aircraft (EOSS) attempts to resolve all the geometric features as shown in Figure 3b. Previously, the grid did not accurately represent the EOSS geometry. In addition, the current grid was designed to allow the EOSS to rotate to any arbitrary position. This capability required extremely fine transitions grids between the EOSS components and the fuselage canopy. The EOSS grids were also designed to facilitate straight forward grid changes in the event of design changes in that region of the fuselage.

The fan-tail grids were modified to improve its representation as shown in Figure 3c. The vertical tail was added which required a number of specialized collar grids to resolve the junctions between the top of the fan-tail and vertical tail and the junction between the vertical and horizontal tails. In the previous computation, the vertical tail was ignored. A center-body was added to the fan-tail to account for the blockage effect and more accurately model the experimental flowfield with the fan-tail powered. The computational centerbody diameter was scaled from photographs of the 15% scale model and the width encompasses the fantail width in the region. The resulting centerbody is a cylinder with a non-dimensional width of 0.0417, diameter of 0.0471, and the edges rounded to 0.25 of the cylinder radius.

Flow Solver Specifics

The flowfields were computed using the general compressible Navier-Stokes flow solver OVERFLOW version 1.6ax by Buning et.al. [6]. This current version of OVERFLOW has a number of flow solver options including implicit time stepping options of Block-Tridiagonal, Penta-Diagonal, and LU/SGS. The spatial differencing options include central differencing with either 2nd and 4th smoothing or various upwind methods. This version is also compatible with various computer platforms, has the ability to perform distributed computations using PVM and is multitasked for concurrent processing on Crays computers.

The flowfield boundary conditions were set using non-reflecting boundaries in the far field. At the surfaces, no slip was imposed and the normal momentum equations were used to obtain surface pressures. At the main rotor plane and fan-tail face, a pressure jump was applied that

averages the density and velocities at two grid planes that lie adjacent to the desired pressure jump location. Half the pressure jump is either added or subtracted to adjacent grid points and the energy variable appropriately computed. For the main rotor, the C_{Trotor} of 0.00509 corresponds to a non-dimensional Δp of 0.00253. The fan-tail thrust of 18.35 lbs_f corresponds to a non-dimensional Δp of 0.022045.

The following computations were run on a Cray YMP-C90 at NASA Ames Research Center's Numerical Aerodynamic Simulation facility. The body forces on the individual grids all converged by 3000 iterations. Each computation required approximately 20 hrs of CPU time on the Cray C90. The computations were typically run with four concurrent processors. On a non-dedicated job queueing system, each case required 12 hours of wall-clock time. The flow solver has a typical compute speed of approximately 6 to 7 microseconds per grid-point per iteration. Each run required a maximum of 22 Mwords of in-core memory.

Results and Comparisons

Flow Fields Particle Traces

Figure 4 illustrates computed particle traces released along fuselage sectional locations at the EOSS, canopy and tail boom locations for the isolated fuselage computations. Overall, the particle paths show a predominately attached flowfield with some local areas of flowfield separation and vortex formations. At the EOSS location, a flowfield separation area exists just behind the EOSS region which results in an unsteady asymmetric flowfield. From the nose to the back of the tail-boom and before the tail-fan area, the flowfield remains mostly attached. Along the tail-boom engine exhaust port regions, a vortex forms, which gets entrained into the fan-tail inlet on the starboard side of the fuselage. As shown in Figure 4b., a vortical flow pattern forms at the exit side of the fan-tail.

Figure 5 illustrates the corresponding particle traces for the fuselage-rotor flow condition. Over the forward part of the fuselage, the flowfield stays mostly attached to the fuselage. At the tail-boom location, the flow forms a highly vortical flow pattern as highlighted in both the starboard and port views. Some of the particles released from the starboard side of the tail-boom are entrained into the fan-tail inlet and exhausted through its exit plane. Other particles released from the tail-boom starboard side flow downwards, mix with particles released from the port side of the tail-boom and then form into a wake that flows primarily behind the port side of the fuselage.

Pressure Comparisons

The pressure comparisons show areas of correlation between the computed and measured surface pressure coefficients. Differences between the computed and measured data can be attributed to either local differences in the geometry or local regions of poor computational grid quality. The major geometric difference is the main rotor hub. The main rotor hub is in both the isolated fuselage and the rotor-fuselages tests. The model support is another major difference and should affect the comparisons along the ventral line and downstream of x/L=0.6. The rotating components of the main rotor and the fan-tail are another geometric difference between the model and computed geometry. The main and fan tail impose a non-uniform pressure jump at their respective rotor disks while the computational geometry uses a uniform pressure jump. There is also a slight geometry difference at the EOSS. In the computational geometry, the EOSS grid was designed to allow the EOSS to rotate to an arbitrary position as in the full scale vehicle. This feature includes a small gap between the EOSS and the forward part of the fuselage canopy. The tunnel model has a fixed position EOSS which blends in with the fuselage.

Keeping these differences in mind, Figure 6 shows a comparison between the measured and computed surface pressures along the symmetry line. The dorsal (upper) surface pressures show a good comparison between the two. The stagnation at the nose of the fuselage and at the engine pylon leading edge are well predicted. The trends along the upper surface of the fuselage from the canopy, through the engine pylon and along the tail boom all correlate well with the data. At the leading edge of the fan-tail, the correlation between the experiment and computed results deviate somewhat. This difference can be attributed to a difference in the grid line positions sampled and the location of the pressure ports.

The ventral (lower) line surface pressure coefficients do not compare as favorably. As before, the stagnation pressures at the fuselage nose and leading edge of the gun mount are well predicted. The trends of the surface pressures up to the gun mount follow the measured data. However, downstream of the engine mount the surface pressures do not correlate well with the experiment. Downstream of the gun mount the surface pressures are rather flat with only a slight pressure gradient. The experimental measurements shows regions of favorable and negative pressure gradients.

The turbulence model can also be source of discrepancy between experimental and computed results. The Baldwin-Lomax [8] turbulence model was used for the above comparisons. This turbulence model may not be well suited for separated flow fields and also is not well suited for overset type grids. The Baldwin-Barth [9] one-equation turbulence model is a much better suited model for such flowfields and grid schemes. Figure 7 shows the dorsal surface pressures obtained for the isolated fuselage case using Baldwin-Lomax and Baldwin-Barth. There is little difference between the two results. The major difference exists in the region where the EOSS joins the canopy. The remaining results use the Baldwin-Barth turbulence model.

Figure 8 shows surface pressure comparisons at three

key fuselage cross sections, EOSS (STA4, x/L=0.04), Canopy (STA11, x/L=0.256) and Tail-Boom (STA22, x/L=0.693). At the EOSS section, the results show similar trends as the experiment above the centerline. Below centerline, the computation overpredicts the pressure. At the canopy sections, the pressures are all over predicted. The pressures follow the same trends as in the experiment above z/L=0.05. But below that line, the pressure do not either follow the measured trends nor do they have similar magnitudes. At the tail-boom section, the surface pressure follows in magnitude the measured pressure values at pressure port locations above the bottom surface. Towards the bottom surface the pressures deviate greatly. The ports at this section are greatly affected by the upstream model post.

Note that all the cross-section plots have oscillations in the surface pressures when the surface geometry has an abrupt change in the slope. These abrupt changes exist throughout the fuselage length. For the stations shown, the EOSS section has abrupt changes at roughly centerline and it exhibits a characteristic pressure fluctuation. The oscillation is also shown in the Canopy section at roughly z/L=0.03. All cross section plots show this behavior and can be controlled by local smoothing of the geometry at these abrupt geometry locations.

In addition, there are some slight pressure oscillations shown in the dorsal and ventral surface pressure distributions. Closer inspection of the flowfield solution revealed either mismatches in grid resolutions at overset grid boundaries or overset grid hole boundaries too close to high gradient flow regions. Both conditions are controllable and require further adjustments to the grid connectivity in order to eliminate the oscillations.

The results for the rotor-fuselage case is shown in Figure 9 and Figure 10. As in the isolated fuselage case, the pressure distributions correlate well to test data in some locations, and fails to correlate in others. The midline dorsal surface pressures shown in Figure 9 show the computed pressures following the measured trends. The stagnation pressures at the fuselage leading edge and at the leading edge of the engine mount are well captured. At both the canopy region and aft of the engine pylon, the pressures have similar trends but the computed pressures underpredict the pressure magnitudes. The differences aft of the engine pylon can be attributed to the main rotor hub.

As before, the computed ventral line surface pressure coefficients do not compare well against the experiment. The stagnation at the fuselage nose and at the leading edge of the gun mount are both well captured along with trends in the surface pressures from the nose up to the gun mount. However, once past the gun mount the computed surface pressure is rather flat with a slight pressure gradient. The measured data on the other hand has relatively large variations.

Three key fuselage cross-sectional pressure distributions at the same locations as in the isolated fuselage case are compared and shown in Figure 10. The EOSS cross section shows an under prediction of the surface pressures compared to the measured data. The canopy cross section shows a much more favorable comparison between the measured and computed results. In the lower part of the cross section ($z/L < 0.03$), the pressure compares well in terms of both magnitude and trend. Greater than 0.03 the pressures follow similar trends but computed results underpredict the test. The tail boom section shows very good correlation. The pressure below z/L=0.04 all match. Above this height, the computed results are again underpredicted.

Summary and Conclusions

In closing, this paper presents a unique comparison between Navier-Stokes solutions and wind-tunnel tests for helicopter fuselage. Comparisons for an isolated fuselage case and for a powered rotor case revealed areas of correlation between the computation and experiment. Geometric differences account for some of the discrepancies between the measured and computed results. In addition, local regions of poor grid quality also added to the errors. Overall, this paper gives confidence to the computational method used and provides flowfield information that can be used to complement wind tunnel data. Further comparisons are required to further investigate the fidelity of the solutions.

References

[1] Duque, E.P.N, and Dimanlig, A.C.B, "Navier-Stokes Simulation of the AH-66 (Comanche) Helicopter", 1994 AHS Aeromechanics Specialists Conference, San Francisco, CA, Jan. 1994.

[2] Luh, R., "Surface Grid Generation for Complex Three-Dimensional Geometries" NASA Technical Memorandum 101046.

[3] Steinbrenner, J.P, Chawner, J.R. and Fouts, C.L., "The GRIDGEN 3-D Multiple Block Grid Generation System, User's Manual", WRDC-TR-90-3022, Wright Research and Development Center.

[4] Chan, W.M. and Steger, J.L., Enhancements of a Three-Dimensional Hyperbolic Grid Generation Scheme, Applied Math and Comp., 51, 181-205, 1992.

[5] Suhs, N.E., and Tramel, R.E., PEGSUS 4.0 Users Manual, Arnold Engineering Development Center, AEDC-TR-91-8, June 1991.

[6] Buning, P., Chan, W., Renze, K., Sondak, K., Chiu, I., and Slotnick, J., OVERFLOW Users Manual Version 1.6ax, May 1995.

[7] Pulliam, T.H. and Chaussee, D.S., A diagonal Form of an Implicit Approximate-Factorization Algorithm, Journal of Computational Physics, Volume 39, Number 2, February 1981.

[8] Baldwin, B.S. and Lomax H., "Thin Layer Approximation and Algebraic Model for Separated Turbulent Flows," AIAA-78-0257, AIAA 16th Aerospace Sciences Meeting, Huntsville, AL, Jan. 1978.

[9] Baldwin, B.S. and Barth T.J, " A One-Equation Turbulence Transport Model for High Reynolds Number Wall Bounded Flows," NASA TM 102847, Aug. 1999

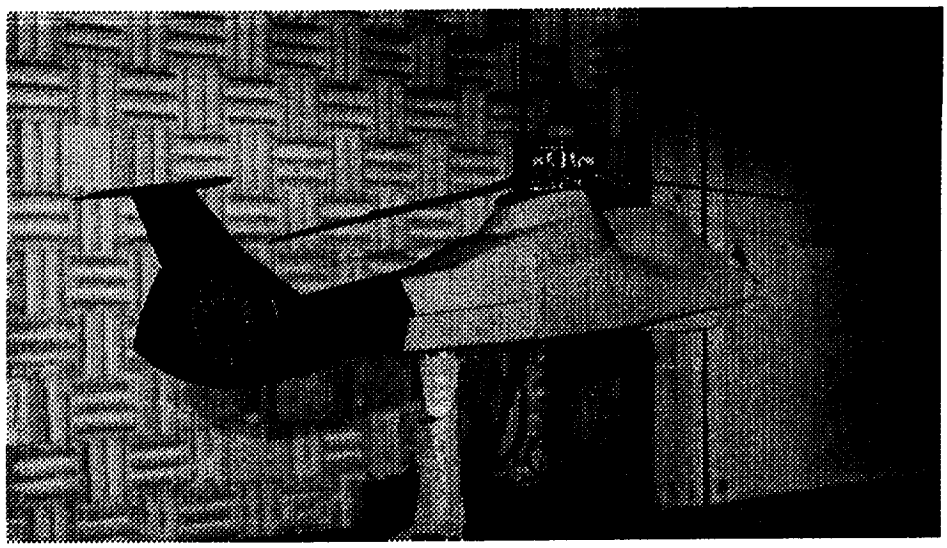

Figure 1 Comanche 15% Scale Model

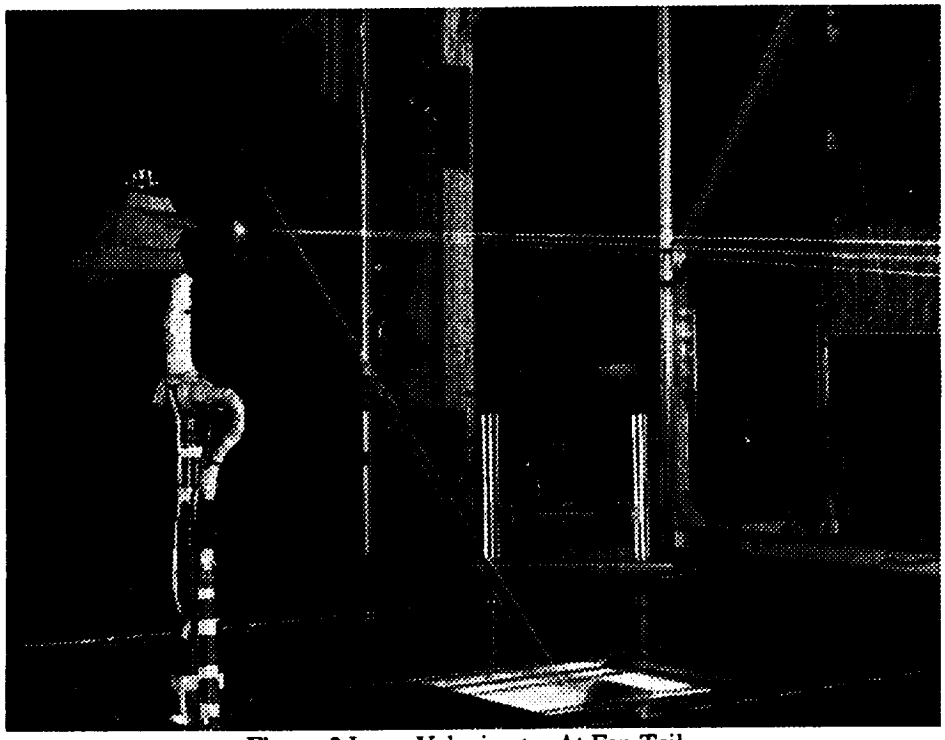

Figure 2 Laser Velocimeter At Fan-Tail

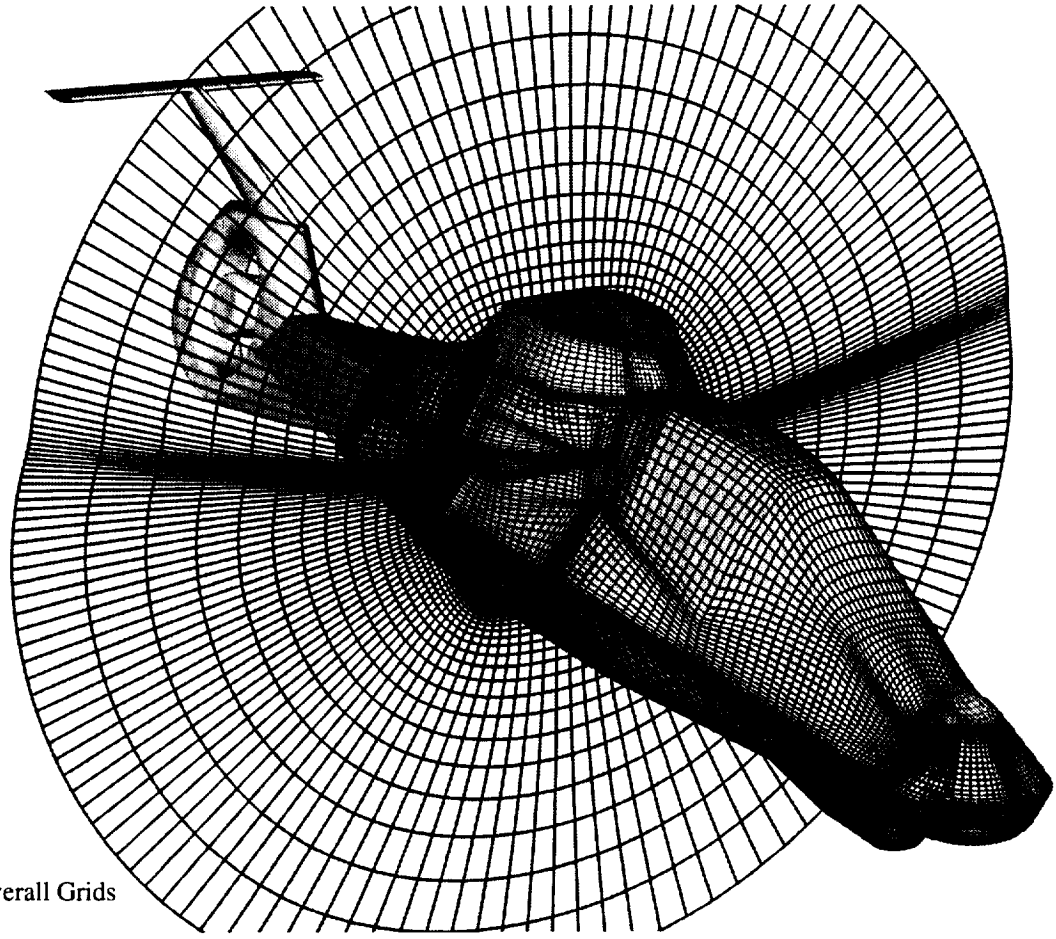

a) Sample Overall Grids

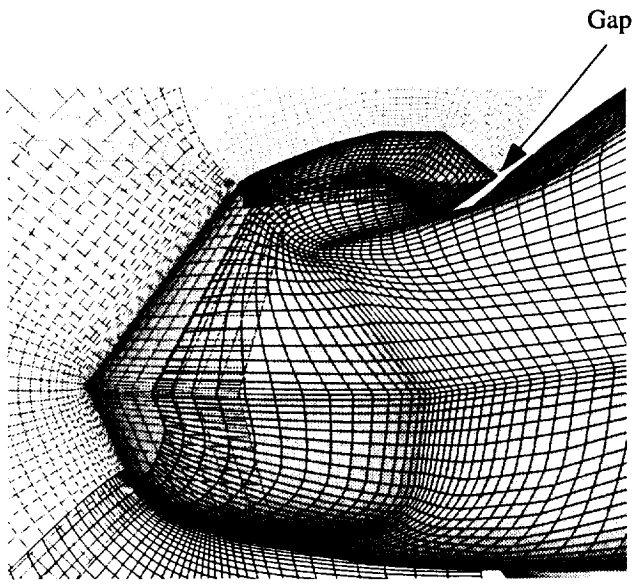

b) EOSS Detail

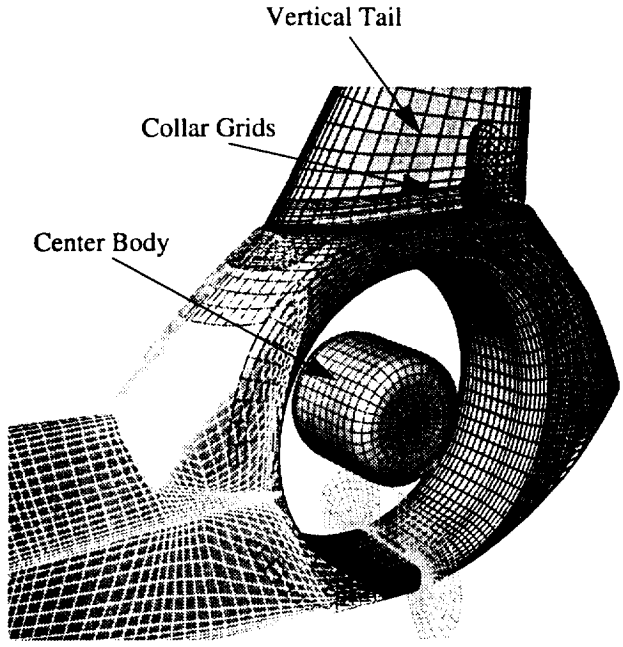

c) Fan-Tail Detail

Figure 3 : Grid Systems Details

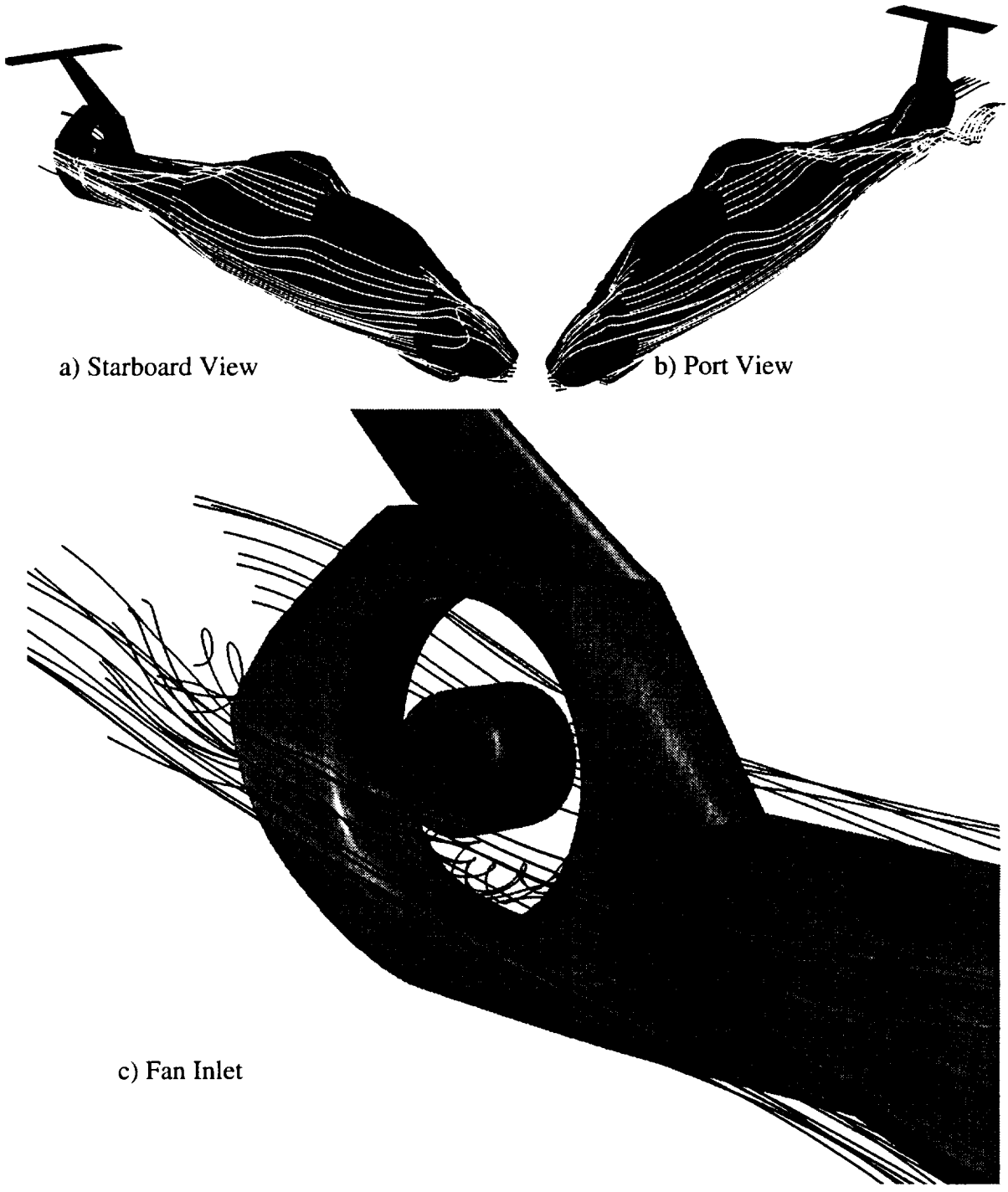

Figure 4 Flow Field Particle Traces, Run 245, Pt 18
Mach = 0.13, Reynolds # = 989,000, $\alpha=0^{o}$,, Fan Thrust = 18.5 lbsf., Isolated Fuselage

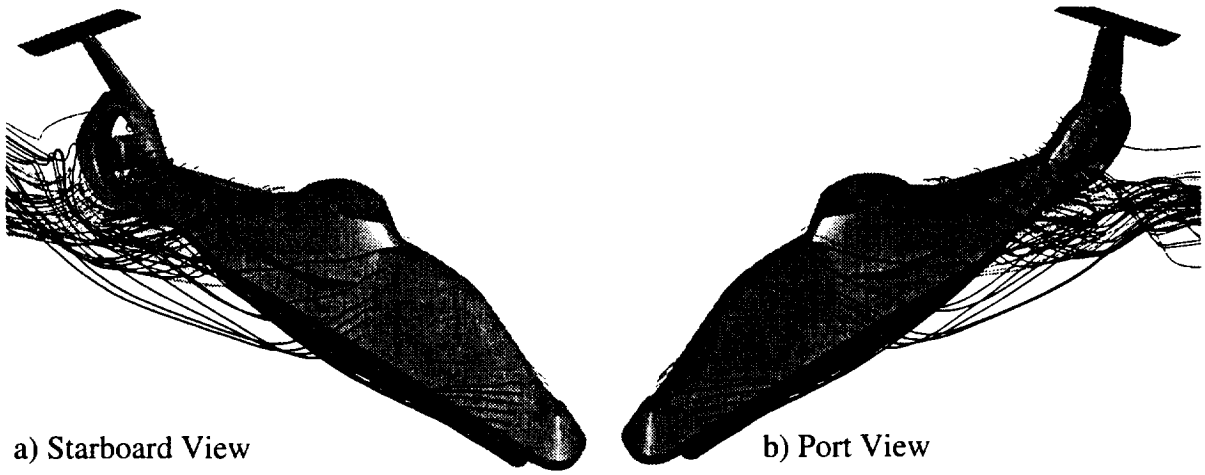

a) Starboard View

b) Port View

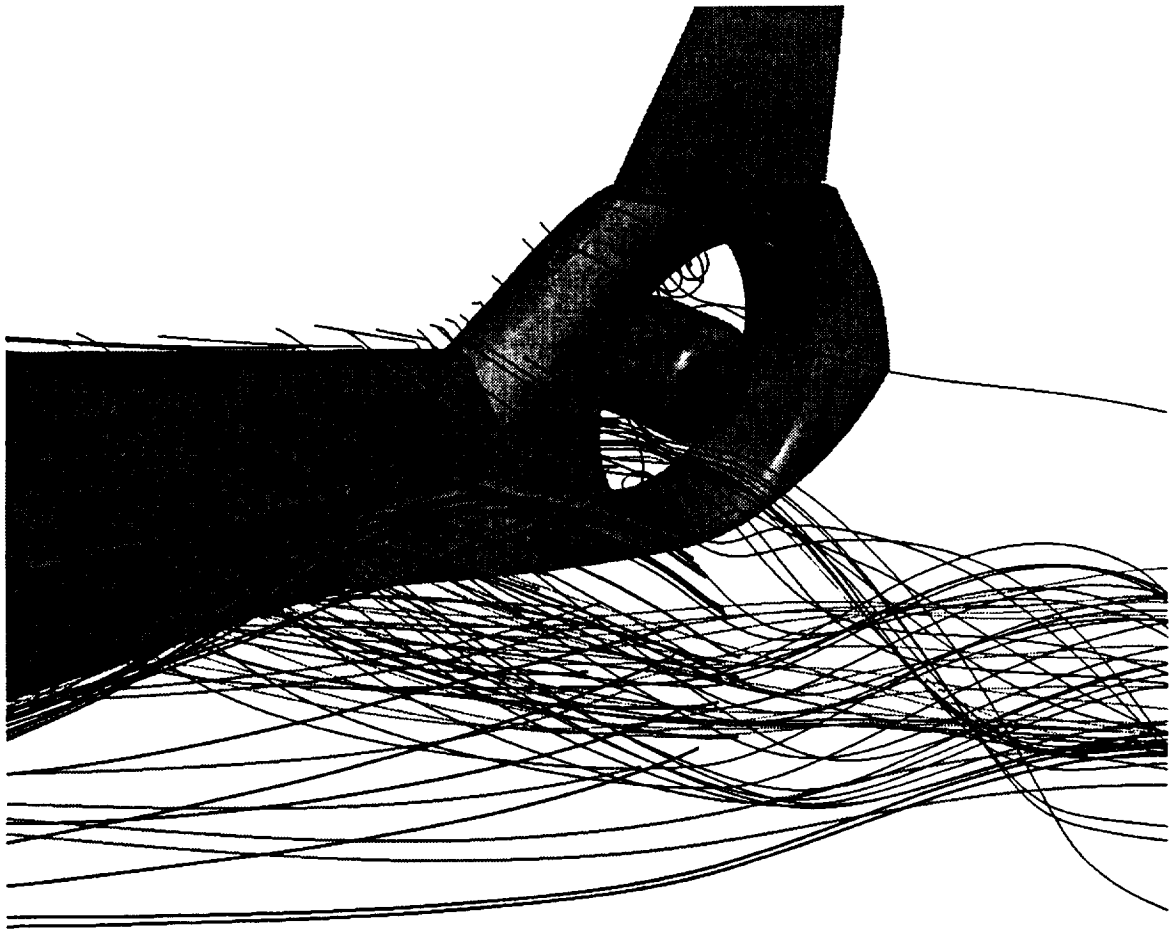

c) Fan Outlet

Figure 5 Flow Field Particle Traces, Run 153 Pt 2
Mach = 0.05, Reynolds # = 367,896, α=-0.737, C_{TRotor} = 0.00509, Fan Thrust = 18.5 lbsf

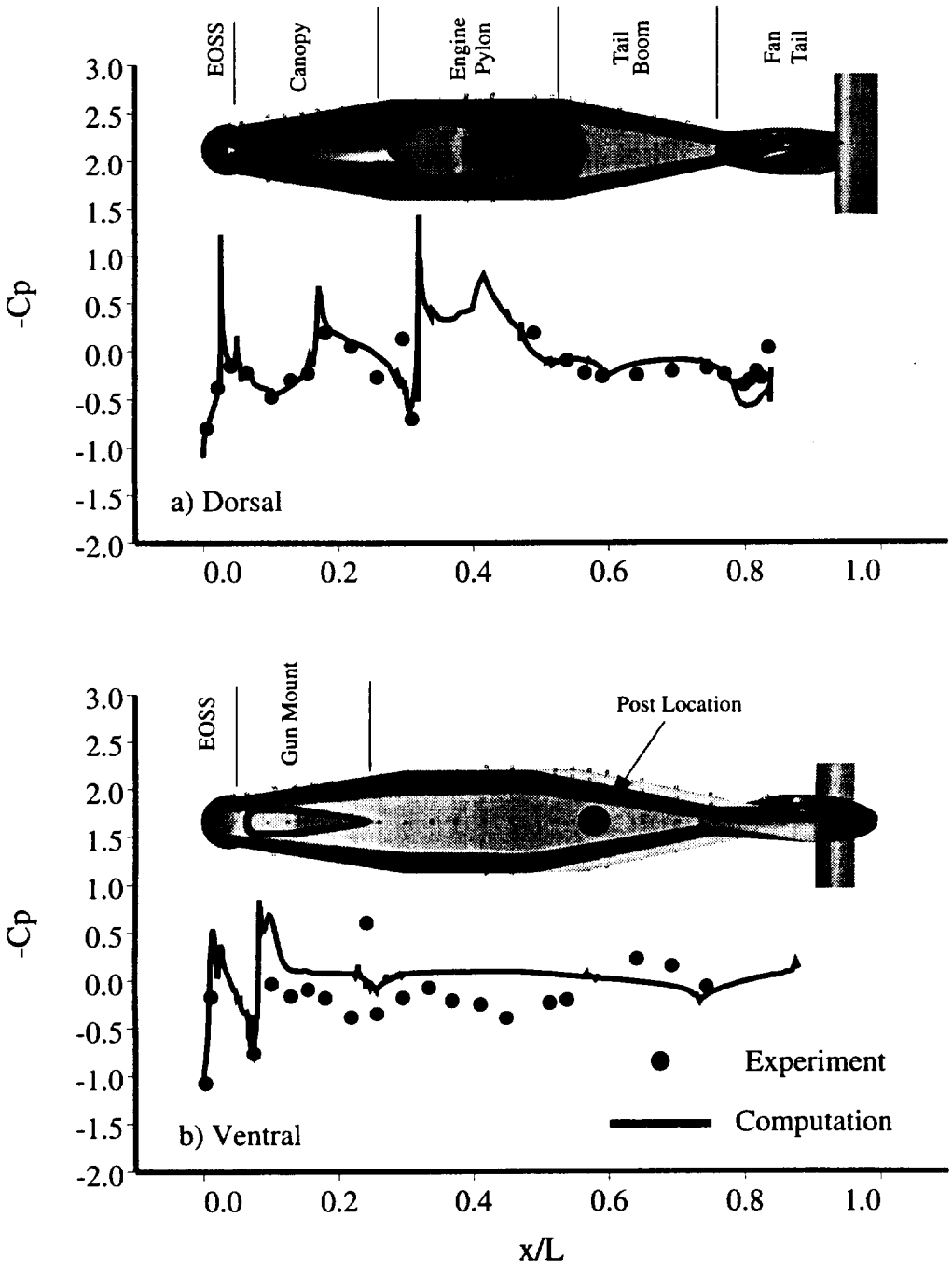

Figure 6 Comparison of Dorsal and Ventral Midline Pressure Coefficients, Run 245, Pt 18, Mach = 0.13, Reynolds # = 989,000, $\alpha=0^{o}$,, Fan Thrust = 18.5 lbsf., Isolated Fuselage

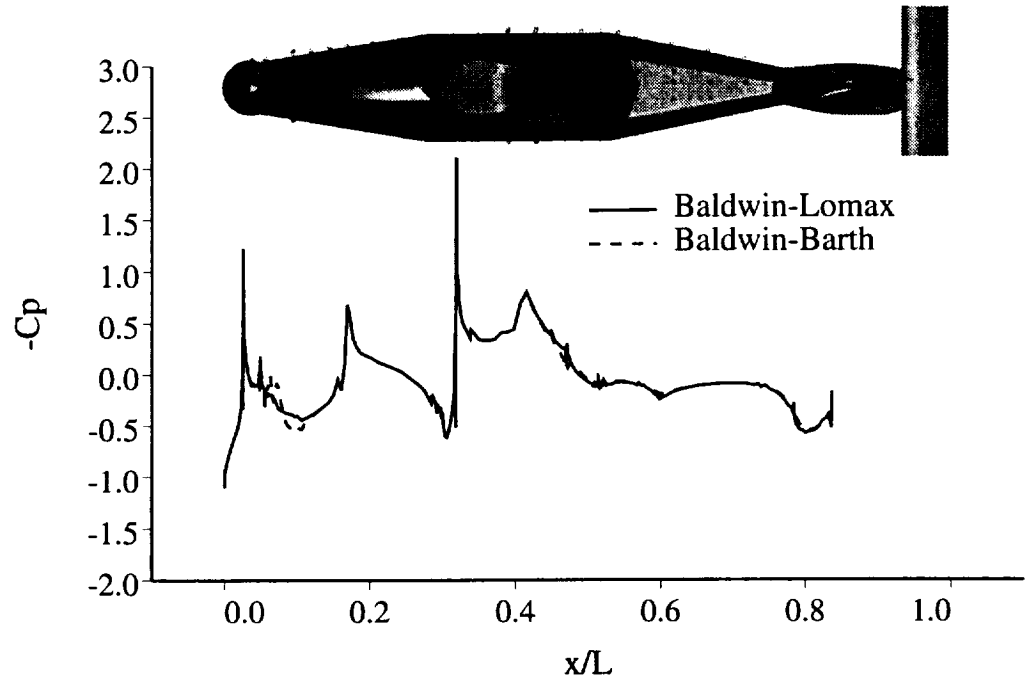

Figure 7 Comparison of Pressure Coefficients Using Baldwin-Barth and Baldwin-Lomax Turbulence Model

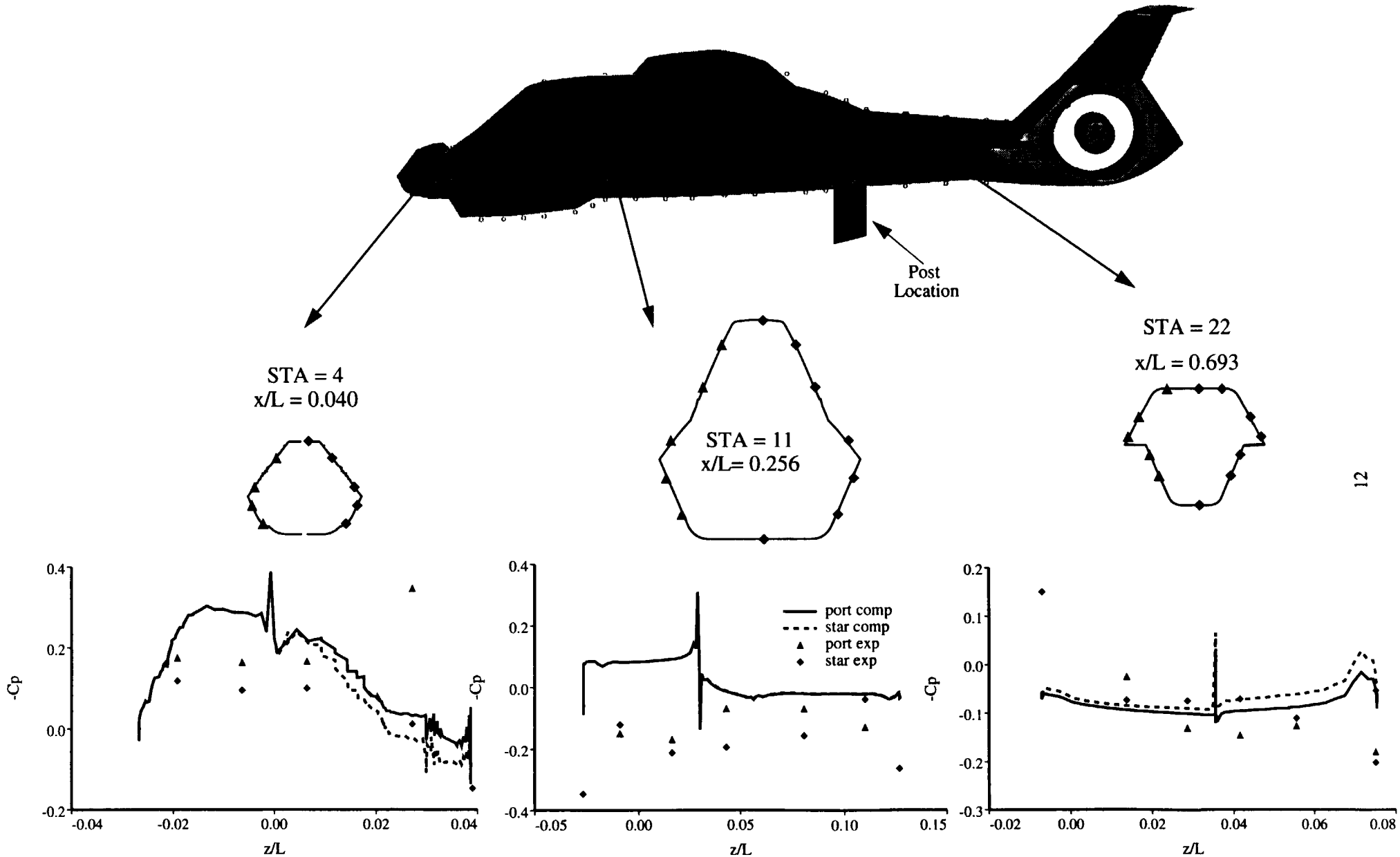

Figure 8 Comparison of Computed and Measured Port and Starboard Pressure Coefficient, Run 245, Pt 18, Mach = 0.13, Reynolds # = 989,000, $\alpha=0^{o}$, Isolated Fuselage, Baldwin-Barth Turbulence Model